Original Article

DOI: 10.5582/bst.2023.01040

Improving the sensitivity of liver tumor classification in ultrasound images *via* a power-law shot noise model

Kenji Karako[1], Yuichiro Mihara[2], Kiyoshi Hasegawa[2], Yu Chen[1,*]

[1] Department of Human and Engineered Environmental Studies, Graduate School of Frontier Sciences, The University of Tokyo, Chiba, Japan;
[2] Artificial Organ and Transplantation Surgery Division, Department of Surgery, Graduate School of Medicine, The University of Tokyo, Tokyo, Japan.

SUMMARY Power laws have been observed in various fields and help us understand natural phenomena. Power laws have also been observed in ultrasound images. This study used the power spectrum of the signal identified from the reflected ultrasound signal observed in ultrasonography based on the power-law shot noise (PLSN) model. The power spectrum follows a power law, which has a scaling factor that depends on the characteristics of the tissue in the region where the ultrasound wave propagates. To distinguish between a tumor and blood vessels in the liver, we propose a classification model that includes a scaling factor based on ResNet, a deep learning model for image classification. In a task to classify 6 types of tissue - a tumor, the inferior vena cava, the descending aorta, the Gleason sheath, the hepatic vein, and small blood vessels – tumor sensitivity increased 3.8% and the F-score for a tumor improved 2% while precision was maintained. The scaling factor obtained using the PLSN model was validated for classification of liver tumors.

Keywords ultrasonography, liver, deep learning, classification, power-law shot noise model

1. Introduction

Power laws occur and are observed in various scientific fields, and they are useful for understanding natural and man-made phenomena. The characteristics of power laws are used in economics and finance, and the scaling factors are used for prediction (*1-3*). The medical field is no exception, and power laws are also observed in ultrasonography.

Ultrasonography is a method widely used to image body tissues because it is relatively safe, versatile, low cost, and mobile. However, ultrasonography has the disadvantages of a low resolution and unclear images compared to other imaging methods such as X-rays, magnetic resonance imaging (MRI), and computerized tomography (CT) scans. One task for which ultrasonography is often used is to diagnose liver cancer. In Japanese guidelines for diagnosis of liver cancer, ultrasonography is the method of choice for screening at-risk patients (*4*). However, pathologists need experience and medical knowledge to accurately diagnose liver cancer. Factors such as contrast-based images, cross-sectional images, and changing shapes depending on the probe angle hamper the identification of parts of the liver in ultrasound images, even with medical knowledge. Experience helps to combine medical knowledge with diverse structures in ultrasound images to correctly understand the intrahepatic region. Despite the convenience of ultrasonography, its drawback is that the examination can only be performed at a large hospital by a liver specialist.

Several studies have sought to determine the features of structures in ultrasound images in order to facilitate a diagnosis (*5-7*). Studies have sought to determine the characteristics of ultrasound waves propagated by a structure using the power-law shot noise (PLSN) model (*8-10*). An ultrasound image is obtained by converting the amplitude of the ultrasound waves emitted by the probe and reflected by structures scattering those waves in a given region into brightness. Previous studies have proposed that the amplitude of this reflected ultrasound wave can be represented by the PSLN model. Since the frequency characteristics of this amplitude follow a power law and the scaling factor of a power law differs depending on the characteristics of the structure propagating waves, they can presumably be used as a feature to distinguish between tissues. A previous study applied this PSLN model to ultrasound images of the breast, allowing breast cancer tissue to be distinguished from normal breast tissue. Such features can presumably be used to aid in diagnosis in areas such as liver cancer that require skill and experience.

At present, the PLSN model has not been applied to ultrasound images other than those of breast cancer.

The current study has focused on the fact that cancer tissue and normal tissue can be distinguished by the PLSN model and that this model can be used to diagnose ultrasound images of liver cancer, a task that requires skill for a precise diagnosis. First, in order to verify whether the PLSN model can be applied to ultrasound images of liver cancer, this study evaluated whether the frequency characteristics reveal the scaling factor according to the power law. Next, this study compared and evaluated whether liver cancer, blood vessels, and liver tissue can be distinguished based on scaling factors. In addition, this study constructed a neural network-based classifier using the scaling factors and it evaluated whether the scaling factors facilitate classification of structures.

The paper is organized as follows. Section 2.1 provides an overview of the PLSN model applied to ultrasonography. Section 2.2, 2.3 provides a method for determining scaling factors for ultrasound images of the liver using the PLSN model. Section 2.4 presents a configuration of a neural network-based classifier using scaling factors. Section 2.5 provides training and evaluation data for the neural network-based classifier. Section 3 provides an evaluation and results for classification of liver cancer, the inferior vena cava, the descending aorta, the Gleason sheath, the hepatic vein, and small blood vessels. Finally, concluding remarks are described in Section 4.

2. Materials and Methods

2.1. The PLSN model for ultrasonography

In ultrasonography, tissues in the body are usually modeled as regions containing randomly distributed structures that scatter ultrasound waves (scatterers), with each one independently affecting backscattering. In the PLSN model, the sum of all such backscattered signals that are received by the transducer is the reflected signal (*10-13*):

$$r(t) = \sum_i h(t, t_i, \boldsymbol{x}_i, \boldsymbol{\psi}_i), \tag{2.1}$$

where t is the time of observation; t_i are the times when independent backscattered pulses $h(\cdot)$ occur and are assumed to be random events taken from a non-homogeneous Poisson process with rate $\lambda(t)$; $\boldsymbol{x}_i$ is the vector denoting the position of the ith scatterer from the transducer; and $\boldsymbol{\psi}_i$ is a random vector that characterizes the amplitude, phase, scale and duration of each backscattered pulse.

Let us focus on reflected signals generated from scatterers at approximately the same depth in tissue. We will also assume that the medium is stationary in the corresponding small segment of tissue and that the scatterer's density, attenuation properties, and medium properties are constant. In addition, we will assume that there are no strong specular reflectors in the scattering region. Based on these assumptions, $\boldsymbol{x}_i$ can be regarded as roughly constant, and the general model in (2.1) can be simplified as follows (*10,12,13*):

$$r(t) = \sum_i h(t - t_i, \boldsymbol{\psi}_i). \tag{2.2}$$

Because of the stationarity assumption, the t_i's $h(\cdot)$ are random events from a homogeneous Poisson process with a constant rate λ. Moreover, since each pulse is a reflected pulse of the ultrasound signal from the probe, it can be assumed to be of the form (*10*):

$$\begin{aligned} h(t - t_i, \boldsymbol{\psi}_i) &= e(t - t_i, a_i)\cos(\omega_c(t - t_i) + \phi_i) \\ &= e_c(t - t_i, a_i)\cos(\omega_c t) - e_s(t - t_i, a_i)\sin(\omega_c t), \end{aligned} \tag{2.3}$$

where $e_c(t\text{-}t_i,a_i)=e(t\text{-}t_i,a_i)\ cos(\phi_i\text{-}\omega_c t_i)$ and $e_s(t\text{-}t_i,a_i)=e(t\text{-}t_i,a_i)\ sin(\phi_i\text{-}\omega_c t_i)$ are respectively the in-phase and quadrature components; ω_c is the center frequency of the ultrasound signal; $e(t\text{-}t_i,a_i)$ is the envelope of the backscattered pulse with a_i specifying its amplitude, and ϕ_i is a random phase. The sum of the scattered signals given by (2.2) is as follows (*10*):

$$r(t) = r_c(t)\cos(\omega_c t) - r_s(t)\sin(\omega_c t),$$

$$r_c(t) = \sum_i e(t - t_i, a_i)\cos(\phi_i - \omega_c t_i), \tag{2.4}$$

$$r_s(t) = \sum_i e(t - t_i, a_i)\sin(\phi_i - \omega_c t_i). \tag{2.5}$$

Furthermore, we will assume that the envelope can be described by (*10,14*):

$$e(t - t_i, a_i) = a_i(t - t_i)^{-\nu}u(t - t_i), \tag{2.6}$$

where $u(t)$ is the unit step function; ϕ_i, a_i, and t_i are respectively assumed to be independent random variables with probability density functions uniform in $[0, 2\pi)$, $f_a(a)=f_a(-a)$, and the Poisson process; and ν is a parameter determined by the characteristics of the area of propagation.

For $0 < \nu \leq 0.5$, research has shown that the sample power spectrum $S(f)$ with regard to $r_c(t)$ or $r_s(t)$ exists and follows a $1/f^{\beta}$ -type behavior with $\beta=2(1\text{-}\nu)$ (*14*), as described by

$$S(f) = \lambda E[a^2]\Gamma^2(\beta/2)(2\pi f)^{-\beta}, \tag{2.7}$$

where $\Gamma(\cdot)$ is the gamma function (*15*), and $E[a^2]$ denotes the expected value of the square of the random amplitude a.

Let $|r(t)| = \sqrt{r_c^2(t) + r_s^2(t)}$ be the envelope of the backscattered signal. The power spectrum of the envelope was derived and has been shown to take a power-law form with exponent β_{env} based on numerical

evaluation (*9*).

In-phase and quadrature components can presumably be obtained from actual data *r(t)* using a Hilbert transform as follows (*9*).

$$r_c(t) = \cos(\omega_c t)\, r(t) + \sin(\omega_c t)\, \bar{r}(t) \quad (2.8)$$

$$r_s(t) = \cos(\omega_c t)\, \bar{r}(t) + \sin(\omega_c t)\, r(t) \quad (2.9)$$

where $\bar{r}(t)$ is the Hilbert transform of *r(t)*. The envelope is obtained by

$$|r(t)| = \sqrt{r_c^2(t) + r_s^2(t)}. \quad (2.10)$$

The above calculation requires the center frequency ω_c of the ultrasound wave. The center frequency changes as the ultrasound wave propagates, and the exact value is not known. Therefore, the following method has been proposed (*9*).

$$\widehat{\omega}_c = 2\pi \frac{\int f S_{\mathrm{nb}}(f) df}{\int S_{\mathrm{nb}}(f) df}, \quad (2.11)$$

Here, $S_{nb}(f)$ denotes the periodogram of the modulated ultrasound signal.

When applying the PLSN model to an actual ultrasound image, the reflected ultrasound signal *r(t)* observed from the probe corresponds to the pixel values on the ultrasound signal path shown in Figure 1. The power spectrum can be obtained by calculating each component based on Equations 2.8-11 and performing a fast Fourier transform.

2.2. Calculation of scaling factors from ultrasound images of the liver

There are three steps in obtaining the scaling factor from the ultrasound image of the liver based on the PLSN model. The first step is the transformation of ultrasound images of the liver and the identification of reflected ultrasound signals. The second step is to calculate the power spectrum of reflected ultrasound signals and to determine scaling factors from the power spectrum following the power law.

In the first step, to obtain the scaling factor based on the PLSN model, the reflected ultrasound signal has to be obtained from the region of propagation. This signal is a signal reflected back to the probe, and the pixel value on the ultrasound image represents the signal as shown in Figure 1. In the previous study that applied the PLSN to ultrasound images of the breast, the path of this reflected signal was in the vertical direction of the image, but in the ultrasound image of the liver, it radiates out from the top of image as shown in Figure 1. In order to determine the radial ultrasound signal, the signal is transformed vertically using piecewise affine transformation as shown in Figure 2. The scikit-image library is used for implementation (*16*). Specifically, the eight points in Figure 2 are correspondingly converted with piecewise affine transformation. The vertical pixel values of the transformed image are used as the reflected ultrasound signal *r(t)* to calculate the scaling factor from step 2 onward.

In the second step, the vertical component is the ultrasound signal *r(t)*, and the cos component $r_c(t)$, sin component $r_s(t)$, and envelope component $|r(t)|$ of the ultrasound signal are calculated based on Equations 2.8-11. The power spectrum is calculated using the periodogram implemented by scipy (*17*) for these three components. Next, for each power spectrum and frequency, the logarithm is calculated. The slope is determined using linear regression provided by scikit-learn (*18*), and this is used as the scaling factor. A sample calculation based on the above is shown in Figure 3. In Figure 3, 300 pixels of continuous data in the direction of the y-axis are identified from the converted ultrasound image as the reflected ultrasound signal *r(t)*, and the power spectrum of the cos component, sin component, and envelope component are calculated and shown in a log-log graph. The slope of the graph is the scaling factor. Figure 3 shows that each component can be plotted as a straight line, although there is a lot of noise

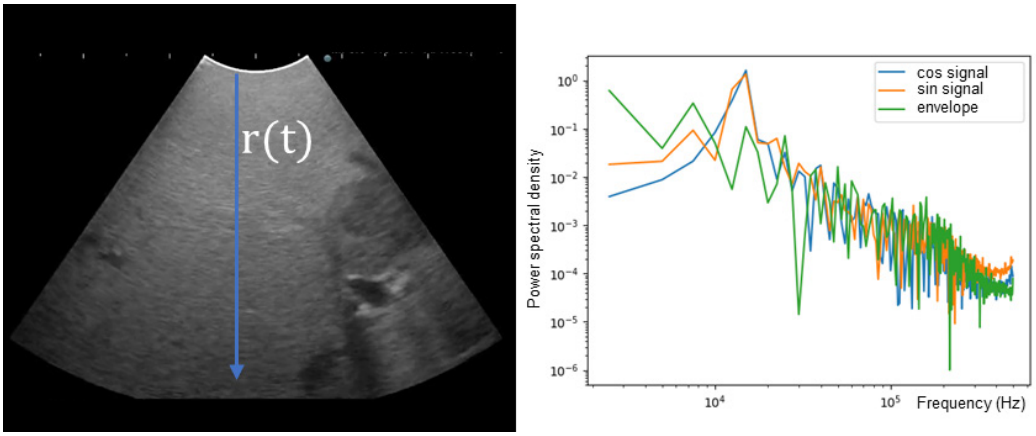

Figure 1. Power spectrum of the reflected ultrasound signal *r(t)* in ultrasound images of the liver incorporating a power-law shot noise model. The power spectrum was calculated for the cos component, sin component, and envelope of the signal.

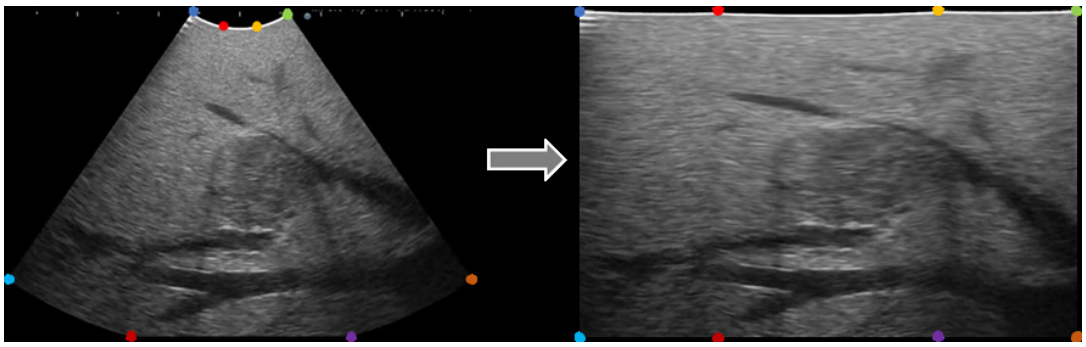

Figure 2. Ultrasound image of the liver transformed by piecewise affine transformation. The direction of signal propagation is unified vertically so that PLSN can be applied to the entire image.

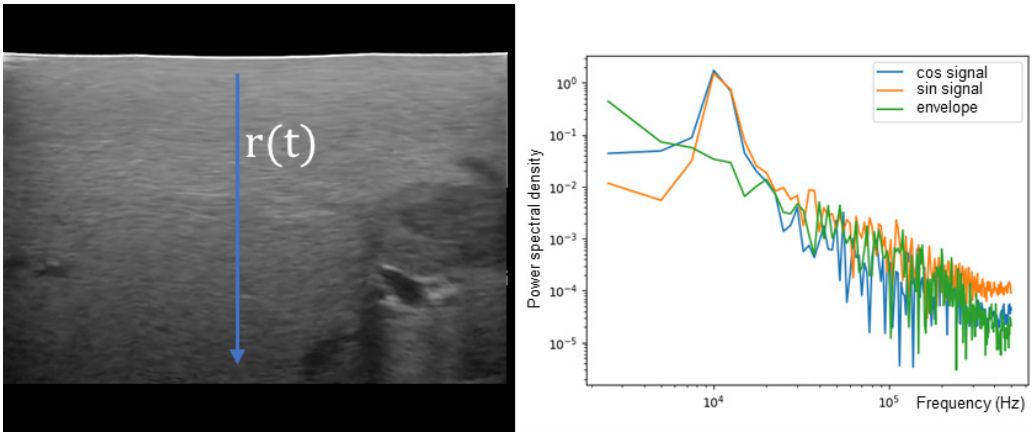

Figure 3. Example of the power spectrum for an image after application of a piecewise affine transformation.

at low and high frequencies, indicating that the power law is obeyed.

2.3. Evaluation of the possibility of distinguishing structures using scaling factors

This section will examine the possibility of distinguishing structures in the liver using scaling factors calculated from actual ultrasound images of the liver. In a previous study, the PLSN model was used to distinguish between cancer tissue and normal breast tissue. Unlike the breast, the liver can contain a tumor as well as the liver parenchyma many blood vessels and other organs. Therefore, the PLSN model has been applied to actual sample data and the frequency characteristics and scaling factors of the calculated reflected waves have been compared. The sample data was from the region indicated in Figure 4 using 3 images including liver cancer and blood vessels. All of the regions were cropped with a width of 50, and 50 reflected ultrasound signals $r(t)$ were included within the region. For each of the 50 signals, the scaling factors for the cos component $r_c(t)$, sin component $r_s(t)$, and envelope component $|r(t)|$ were calculated, and the average of the 50 signals is shown in the Table 1. This study was approved by the institutional review board of the Graduate School of Medicine and Faculty of Medicine, The University of Tokyo (no. 2019166NI), and informed consent was obtained in the form of an opt-out on the website. All data were obtained from ultrasound images taken during an intraoperative ultrasound as part of liver cancer screening. All images used in this study were obtained from three patients with liver cancer and two donors with normal livers.

A comparison of the scaling factors for the cos and sin signals of the liver parenchyma in Table 1 to the scaling factors of other structures reveals that the liver parenchyma and other structures can be distinguished with a scaling factor less than 1.8. In contrast, tumors and blood vessels are difficult to distinguish with a scaling factor of 1.8 or higher. The large standard deviation indicates that the scaling factor obtained varies depending on the location of its acquisition.

2.4. A deep neural network model for ultrasound image classification using a scaling factor map

As shown in 2.3, the scaling factors obtained from the PLSN model were found to have some utility as discriminative indices. However, the scaling factors obtained vary greatly depending on the position, precluding their use alone to identify tumors and blood vessels. Therefore, a scaling factor map was generated

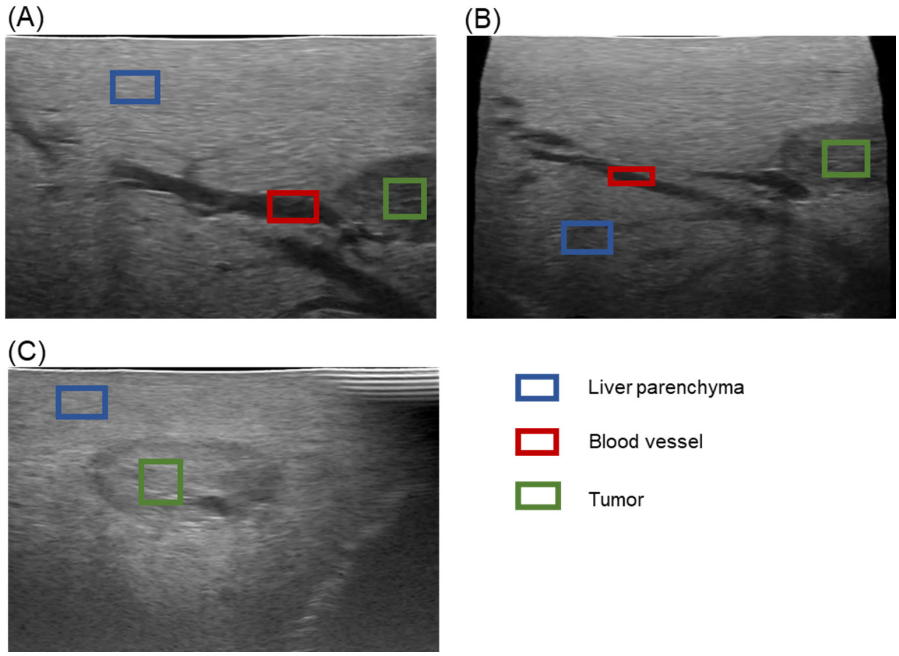

Figure 4. Regions of the liver parenchyma, blood vessels, and a tumor for scaling factor comparisons using the PLSN model. Vertical pixel information within each rectangle is used for comparison. Each region contains 50 ultrasound signals.

Table 1. Average of scaling factors calculated for the liver parenchyma, blood vessels, and tumors

Structure	Scaling factor		
	cos signal	sin signal	envelope
Blood vessel (A)	2.75 ± 0.83	2.11 ± 0.49	1.84 ± 0.55
Blood vessel (B)	2.21 ± 0.87	2.19 ± 0.84	2.34 ± 0.89
Tumor (A)	2.06 ± 0.66	1.93 ± 0.87	2.26 ± 0.47
Tumor (B)	1.94 ± 0.70	1.97 ± 0.63	2.00 ± 0.26
Tumor (C)	2.28 ± 0.55	2.09 ± 0.55	1.88 ± 0.41
Liver parenchyma (A)	1.32 ± 0.87	0.99 ± 0.56	1.28 ± 0.23
Liver parenchyma (B)	1.77 ± 0.67	1.36 ± 0.67	2.12 ± 0.39
Liver parenchyma (C)	1.72 ± 0.68	1.69 ± 0.67	1.28 ± 0.30

from ultrasound images in which local scaling factors were calculated for each coordinate. Proposed here is a model in which this scaling factor map and ultrasound images are combined to classify structures in the liver.

The scaling factor map is generated based on ultrasound images with the piecewise affine transformation described in 2.2. Let $r_{i,j}$ be the pixel value at coordinate *(i,j)*. The scaling factors for the cos component $r_c(t)$, sin component $r_s(t)$, and envelope component $|r(t)|$ are calculated using the value of $r_{i,j}$ to $r_{i,j+T}$ as the ultrasound signal $r_{i,j}(t)$, where T is the size of the clipping window. Each calculated scaling factor is used as a new pixel value $(\beta_{cos},\beta_{sin},\beta_{envelope})$ at *(i,j)*. Let the size of the original ultrasound image be $W \times H$. The scaling factor map is generated by performing this calculation in the region $W \times H - T$. A sample generated by this process is shown in Figure 5.

Image classification is accomplished by training an image classification deep neural network with both the scaling factor map obtained as described above and an original ultrasound image of size $W \times H - T$. ResNet-50 (*19*) has been used as the model of the deep neural network since it has exhibited excellent performance for the image classification involving 100 classes, known as CIFAR-100 (*20*). While ResNet-50 normally learns from normal images (images consisting of three types of information RGB: red, green, and blue), the proposed method uses 5 channels of RGB plus cos scaling factor β_{cos} and envelope scaling factor $\beta_{envelope}$. The reason why the sin component is not used here is that theoretically, the sin scaling factor β_{sin} and scaling factor β_{cos} are the same value, and the more information input in the neural network model, the more likely it is to become noise. The structure of the constructed model is shown in Figure 6. ResNet-50 is implemented using a model provided by PyTorch (*21*). A transfer learning method that utilizes a model that has previously been trained with CIFAR-100 in used during training. In this instance, the input layer is discarded because the learning model has 3 channels of RGB information in the input layer; the current model has been changed to receive 5 channels of information. Adam is used for learning, and a cross-entropy loss

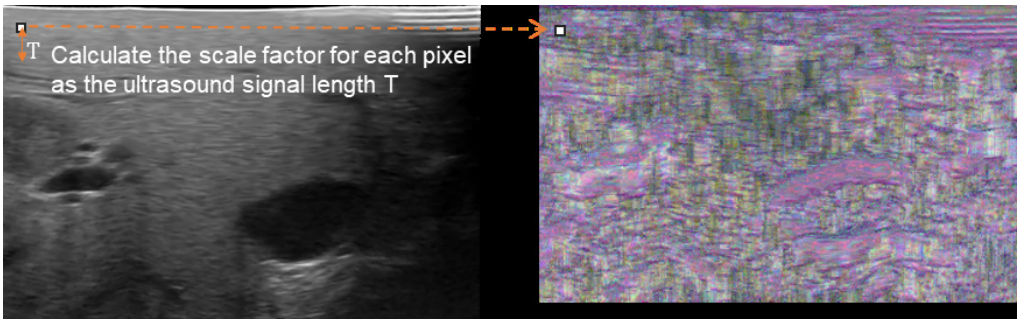

Figure 5. Conversion of an ultrasound image to a scaling factor map with a crop window size of *T=40*. The scaling factor map depicts the scaling factors for the cos, sin, and envelope components as a three-color image.

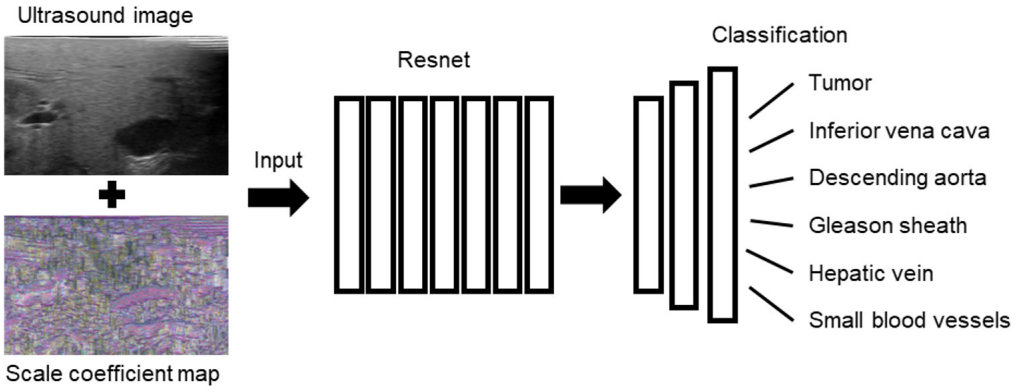

Figure 6. Configuration of a neural network for classification of structures in the liver, using ResNet-50 as a base model to identify features from the input ultrasound images and scaling factor maps. In the output layer, a feedforward neural network is used to predict 6 types of structures.

function is used as the loss function for classification.

2.5. Training and evaluation data from ultrasound images of the liver

To provide training and evaluation data for the proposed model, six types of structures in ultrasound images of the liver were labeled by an experienced physician based on the data described in 2.3: a tumor, the inferior vena cava, the descending aorta, the Gleason sheath, the hepatic vein, and small blood vessels. Sample images of the various structures are shown in Figure 7. For the training and evaluation data for the classification task, the image shown in Figure 7 is used instead of the entire image shown in Figure 5. In the cropped image, the region containing the structure is identified and only the target structure is included as much as possible. In addition, scaling factor maps are also used for learning and evaluation by cropping the ultrasound images according to their size. These sets of ultrasound images and scaling factor maps were obtained for each structure in the liver and their label information was used as learning and evaluation data. The training data obtained by the above method consisted of a total of 3,349 structures, including 251 tumors, 207 inferior vena cavas, 168 descending aortas, 1269 Gleason sheaths, 1145 hepatic veins, and 309 small blood vessels. Similarly, the data for evaluation

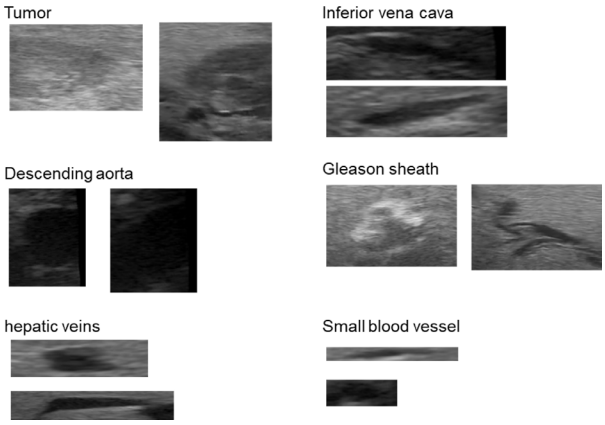

Figure 7. Sample images of a tumor, the inferior vena cava, the descending aorta, the Gleason sheath, the hepatic vein, and small blood vessels to be used as training and evaluation data. Scaling factor maps cropped to fit each image size are also used as input for the neural network.

consisted of a total of 770 structures, including 78 are tumors, 44 inferior vena cavas, 29 descending aortas, 264 Gleason sheaths, 277 hepatic veins, and 78 small blood vessels.

3. Results

To evaluate the performance of the proposed

classification model using scaling factors, the proposed model was trained using a classification task involving 6 types of structures in the liver using the training data described in 2.5. The proposed model was compared to a model trained on ultrasound images alone as input for the classification task. The evaluation data described in 2.5 were used to evaluate performance. To prevent overlearning of the data, noise addition, which is often used as a general method of data expansion, was used when training data for both models. The size of the cropping window T for the scaling factor map was 40, batch size during training was 128, total training epochs was 400, and Adam, a commonly used method of optimization, was used. Figures 8 show the changes in accuracy for all labels in each learning epoch. The performance index was calculated every 10 epochs.

The accuracy in Figure 8 indicates that learning is calmer after 300 epochs. The mean values of each performance indicator over 300 to 400 epochs are shown in Table 2. Table 2 shows that the overall accuracy decreased by 0.017 when ResNet-50 was compared to the proposed model. That said, the proposed model improved the sensitivity by 0.038 and it improved the F-score by 0.020 while maintaining precision with regard to tumor identification.

4. Discussion

The results in 2.3 demonstrate that the PLSN model can be used not only to distinguish cancer tissue from normal tissue in the breast, as reported in a previous study, but it can also distinguish between intrahepatic structures and the liver parenchyma, since the power law was observed in the ultrasound images of the liver. The scaling factor, which is expected to be an indicator with which to distinguish structures, can easily distinguish between the liver parenchyma and other structures (tumors and blood vessels), but it has difficulty clearly distinguishing between tumors and blood vessels because of the large variation in scaling factors depending on the location. One reason for the large variation is that the power spectrum of the reflected ultrasound signal calculated using the PLSN model contains a lot of noise at low and high frequencies, as shown in Figure 3. The scaling factor is the slope of the power spectrum, and its value is presumably greatly affected by noise. Due to this noise, there is a large standard deviation in the scaling factor for the same structure based on the ultrasound signal even though the regions used for verification in 2.3 were selected so that they all consisted of a single structure (a tumor, a blood vessel, or the liver parenchyma).

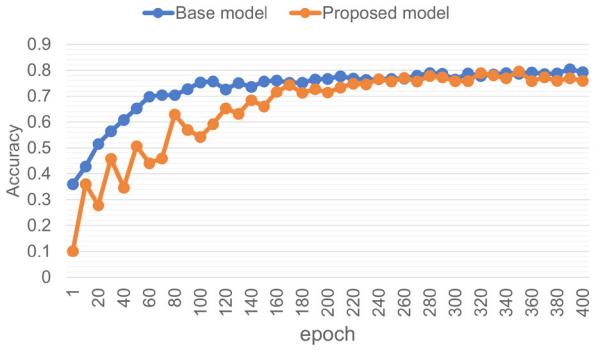

Figure 8. Accuracy per 10 epoch for all labels.

Since distinguishing between structures in the liver is difficult using scaling factors alone, a predictive model was constructed in 2.4 using a combination of ultrasound images and the scaling factor map. Its effectiveness was examined in 3, and the proposed model improved the sensitivity for a tumor, but the overall accuracy was lower than when only image data were used. The inclusion of a scaling factor improved sensitivity by 3.8% and the F-score by 2.0% for a tumor, and it improved precision by 6.7% and F-score by 2.8% for the inferior vena cava. For the descending aorta and Gleason sheath, precision and sensitivity improved but F-scores decreased. For the hepatic vein and small blood vessels, both precision and sensitivity and F-scores decreased. The detection of tumors is particularly important in ultrasonography. In this respect, the proposed model with scaling factors was effective at identifying intrahepatic tumors. Structures (a tumor, the inferior vena cava, the descending aorta, and the Gleason sheath) that were identified with increased precision or sensitivity had several features in common: they were circular in shape and larger than the hepatic

Table 2. Overall mean accuracy and precision, sensitivity, and F-score per epoch for each label averaged over 300 to 400 epochs. Superior values from the two models are shown in bold. The proposed model had improved tumor sensitivity while maintaining precision

	Base model			Proposed model		
Overall accuracy	**0.789**			0.772		
	Precision	Sensitivity	F-score	Precision	Sensitivity	F-score
Tumor	0.951	0.879	0.913	0.951	**0.917**	**0.933**
Inferior vena cava	0.879	**0.980**	0.925	**0.946**	0.961	**0.953**
Descending aorta	0.936	**1.000**	**0.966**	**0.960**	0.952	0.955
Gleason sheath	**0.808**	0.769	**0.787**	0.745	**0.816**	0.777
Hepatic vein	0.740	**0.810**	**0.773**	0.768	0.737	0.748
Small blood vessel	**0.646**	**0.506**	**0.561**	0.555	0.423	0.462

vein and small vessels. Currently, scaling factors are calculated by identifying ultrasound signals with a fixed length of 40 px in the vertical direction. When the structure is small, and especially when it has a short y-axis like the hepatic vein, the signal propagating through the structure and also the signal from the liver parenchyma and other structures are identified and the scaling factor is calculated, which adversely affects classification. Therefore, use of a particular method of ultrasound signal identification depending on the region would allow the exclusion of regions with different scaling factors during classification. Object detection models such as Faster R-CNN (*22*), Mask R-CNN (*23*), and YOLO (*24*) could be used to select the region. In fact, several studies have examined the detection of tumors in regions of ultrasound images (*25,26*), and a combination of this approach and scaling factors could further improve classification sensitivity with regard to tumors.

The PLSN model had previously been validated only for ultrasound images of breast cancer. However, the current study tested whether the PLSN model is also valid for ultrasound images of liver tumors. Results indicated that the liver parenchyma and other structures (tumor and blood vessels) can be distinguished based on the scaling factors calculated using the PLSN model. In addition, a classification model was proposed in which the scaling factor map is combined with a deep learning model to further distinguish intrahepatic structures. Validation with six types of structures (a tumor, the inferior vena cava, the descending aorta, the Gleason sheath, the hepatic vein, and small blood vessels) indicated that the sensitivity of tumor detection improved.

Funding: This study was supported by the Japan Society for the Promotion of Science (JSPS) KAKENHI Grant 20K20492 (Kumiko TANAKA-Ishii and Yu Chen).

Conflict of Interest: The authors have no conflicts of interest to disclose.

References

1. Bouchaud JP. Power laws in economics and finance: Some ideas from physics. Quant. Finance. 2001; 1:105-112.
2. Gabaix X. Power laws in economics and finance. Annu. Rev. Econ. 2009; 1:255-293.
3. Gabaix X. Power laws in economics: An introduction. J Econ Perspect. 2016; 30:185-205.
4. Kokudo N, Takemura N, Hasegawa K, Takayama T, Kubo S, Shimada M, *et al*. Clinical practice guidelines for hepatocellular carcinoma: The Japan Society of Hepatology 2017 (4th JSH-HCC guidelines) 2019 update. Hepatol Res. 2019; 49:1109-1113.
5. Qi X, Yi F, Zhang L, Chen Y, Pi Y, Chen Y, Pi Y, Chen Y, Guo J, Wang J, Guo Q, Li J, Chen Y, Lv Q, Yi Z. Computer-aided diagnosis of breast cancer in ultrasonography images by deep learning. Neurocomputing. 2022; 472:152-165.
6. Yi J, Kang HK, Kwon JH, Kim KS, Park MH, Seong YK, Kim DW, Ahn B, Ha K, Lee J, Hah Z, Bang WC. Technology trends and applications of deep learning in ultrasonography: image quality enhancement, diagnostic support, and improving workflow efficiency. Ultrasonography. 2021; 40:7-22.
7. Ozaki J, Fujioka T, Yamaga E, Hayashi A, Kujiraoka Y, Imokawa T, Takahashi K, Okawa S, Yashima Y, Mori M, Kubota K, Oda G, Nakagawa T, Tateishi U. Deep learning method with a convolutional neural network for image classification of normal and metastatic axillary lymph nodes on breast ultrasonography. Jpn J Radiol. 2022; 40:814-822.
8. Petropulu AP, Golas T, Vishwanathan G. Power-law shot noise and its application on modeling of ultrasound echoes. In: Proceedings of the IEEE-SP International Symposium on Time-Frequency and Time-Scale Analysis. 1998; 193-196.
9. Kutay MA, Petropulu AP, Piccoli CW. On modeling biomedical ultrasound RF echoes using a power-law shot-noise model. IEEE Trans Ultrason Ferroelectr Freq Control. 2001; 48:953-968.
10. Kutay MA, Petropulu AP, Piccoli CW. Breast tissue characterization based on modeling of ultrasonic echoes using the power-law shot noise model. Pattern Recognit Lett. 2003; 24:741-756.
11. Wagner RF, Insana MF, Brown DG. Unified approach to the detection and classification of speckle texture in diagnostic ultrasound. Opt Eng. 1986; 25:256738-256738.
12. Sleefe GE, Lele PP. Tissue characterization based on scatterer number density estimation. IEEE Trans Ultrason Ferroelectr Freq Control. 1988; 35:749-757.
13. Chen JF, Zagzebski JA, Madsen EL. Non-Gaussian versus non-Rayleigh statistical properties of ultrasound echo signals. IEEE Trans Ultrason Ferroelectr Freq Control. 1994; 41:435-440.
14. Lowen SB, Teich MC. Power-law shot noise. IEEE Trans Inf Theory. 1990; 36:1302-1318.
15. Zwillinger D. 12 - Fourier, Laplace, and Mellin transforms. In: Table of Integrals, Series, and Products (Moll V, Gradshteyn IS, Ryzhik IM, eds.). Boston, 2014; pp. 1077-103.
16. scikit-image, Piecewise Affine Transformation — skimage v0.20.0.dev0 docs. *https://scikit-image.org/docs/dev/auto_examples/transform/plot_piecewise_affine.html* (Accessed March 12, 2023).
17. SciPy. scipy.signal.periodogram — SciPy v1.8.0 Manual. *https://docs.scipy.org/doc/scipy/reference/generated/scipy.signal.periodogram.html* (Accessed March 12, 2023).
18. Scikit-learn. sklearn.linear_model.LinearRegression. *https://scikit-learn.org/1.2/modules/generated/sklearn.linear_model.LinearRegression.html* (Accessed March 12, 2023).
19. He K, Zhang X, Ren S, Sun J. Deep residual learning for image recognition. In: Proc. IEEE Comput Soc Conf Comput Vis Pattern Recognit. 2016; 770-778. doi:10.1109/CVPR.2016.90.
20. Krizhevsky A, Hinton G, others. Learning multiple layers of features from tiny images. 2009.
21. PyTorch. ResNet | PyTorch. *https://pytorch.org/hub/pytorch_vision_resnet/* (Accessed March 12, 2023).
22. Ren S, He K, Girshick R, Sun J. Faster R-CNN: Towards real-time object detection with region proposal networks. IEEE Trans Pattern Anal Mach Intell. 2017; 39:1137-1149.

23. He K, Gkioxari G, Dollár P, Girshick R. Mask R-CNN. In: 2017 Proc IEEE Int Conf Comput Vis. 2017; 2980-2988.
24. Redmon J, Farhadi A. Yolov3: An incremental improvement. 2018, arXiv preprint. https://doi.org/10.48550/arXiv.1804.02767
25. Karako K, Mihara Y, Arita J, Ichida A, Bae SK, Kawaguchi Y, Ishizawa T, Akamatsu N, Kaneko J, Hasegawa K, Chen Y. Automated liver tumor detection in abdominal ultrasonography with a modified faster region-based convolutional neural networks (Faster R-CNN) architecture. Hepatobiliary Surg Nutr. 2022; 11:675-683.
26. Nakashima T, Tsutsumi I, Takami H, Doman K, Mekada Y, Nishida N, Kudo M. A study on liver tumor detection from an ultrasound image using deep learning. Proceedings of the SPIE. 2020; 11515.

Received March 7, 2023; Revised March 31, 2023; Accepted April 5, 2023

*Address correspondence to:
Yu Chen, Department of Human and Engineered Environmental Studies, Graduate School of Frontier Sciences, The University of Tokyo, 5-1-5 Kashiwanoha, Kashiwa Chiba 227-8568, Japan.
E-mail: chen@edu.k.u-tokyo.ac.jp

Released online in J-STAGE as advance publication April 13, 2023.